scientific reports

Check for updates

OPEN

Design and analysis for the SPICE parameters of waveform-selective metasurfaces varying with the incident pulse width at a constant oscillation frequency

Shiori Imai[1], Haruki Homma[2], Kairi Takimoto[2], Mizuki Tanikawa[2], Jin Nakamura[3], Masaya Kaneko[3], Yuya Osaki[3], Kiichi Niitsu[4], Yongzhi Cheng[5], Ashif Aminulloh Fathnan[2] & Hiroki Wakatsuchi[2]✉

In this study, we numerically demonstrate how the response of recently reported circuit-based metasurfaces is characterized by their circuit parameters. These metasurfaces, which include a set of four diodes as a full wave rectifier, are capable of sensing different waves even at the same frequency in response to the incident waveform, or more specifically the pulse width. This study reveals the relationship between the electromagnetic response of such waveform-selective metasurfaces and the SPICE parameters of the diodes used. In particular, we draw conclusions about how the SPICE parameters are related to (1) the high-frequency operation, (2) input power requirement and (3) dynamic range of waveform-selective metasurfaces with supporting simulation results. First, we show that reducing a parasitic capacitive component of the diodes is important for realization of the waveform-selective metasurfaces in a higher frequency regime. Second, we report that the operating power level is closely related to the saturation current and the breakdown voltage of the diodes. Moreover, the operating power range is found to be broadened by introducing an additional resistor into the inside of the diode bridge. Our study is expected to provide design guidelines for circuit-based waveform-selective metasurfaces to select/fabricate optimal diodes and enhance the waveform-selective performance at the target frequency and power level. Our results are usefully exploited to ensure the selectivity based on the pulse duration of the incident wave in a range of potential applications including electromagnetic interference, wireless power transfer, antenna design, wireless communications, and sensing.

Artificially engineered structures referred to as metamaterials and metasurfaces enable ready tailoring of electromagnetic fields at will[1–5]. Compared to conventional materials that respond to an incident wave in accordance with the reaction of composite molecules, the response of metasurfaces is characterized by composite unit cells that are much larger than molecules but still at the subwavelength scale and can thus be arbitrarily customized to achieve a range of electromagnetic properties including negative refraction[6] and a large impedance surface[3]. In addition, these metasurfaces with exotic properties can be exploited to develop applied devices or systems such as invisibility cloaks[7,8], diffraction-limit-breaking lenses[9,10], perfect absorbers[11–14], antennas[15,16], analogue computation systems[17–19] and beamforming systems[4,5,20–22] as intelligent reflecting surfaces (IRSs)[23–25].

In particular, these artificially constructed materials attain a higher performance level by including nonlinearity, which offers capabilities that are not available with a simple combination of linear media or structures[26–29]. For instance, nonlinear metasurface-based absorbers dissipate the energy of a strong electromagnetic wave to

[1]Department of Electrical and Mechanical Engineering, Faculty of Engineering, Nagoya Institute of Technology, Nagoya, Aichi 466-8555, Japan. [2]Department of Engineering, Graduate School of Engineering, Nagoya Institute of Technology, Nagoya, Aichi 466-8555, Japan. [3]Kyoto Engineering Center, Meitec Corporation, Kyoto 600-8216, Japan. [4]Graduate School of Informatics, Kyoto University, Kyoto 606-8501, Japan. [5]School of Information Science and Engineering, Wuhan University of Science and Technology, Wuhan 430081, China. ✉email: wakatsuchi.hiroki@nitech.ac.jp

prevent electromagnetic interference issues while permitting propagation of a small signal for antenna communication even at the same frequency[30–33]. Also, nonlinear metasurfaces can be designed as intensity-dependent surfaces allowing various functionalities including spatial wave control[34–36], switchable transmission[37] and digitally defined beam deflection[38]. Additionally, the electromagnetic response of nonlinear metasurfaces or IRSs is altered in accordance with surrounding electromagnetic fields or incoming communication signals, which is achieved by including nonlinear circuit elements together with a field-programmable gate array (FPGA) and an external direct current (DC) source[39,40].

Moreover, a series of recent studies demonstrated that metasurfaces composed of Schottky diodes were capable of sensing different waves even at the same frequency in response to the incoming waveform, or more specifically the pulse width[41–44]. This waveform selectivity provides a new degree of freedom to control electromagnetic waves at a single frequency, which has thus far been exploited to mitigate electromagnetic interference[44], design antennas[45–47] and related microwave devices[48,49] and control communication signals[43,50,51]. Although the electromagnetic response related to the conducting geometry is well known to be improved by existing methods, including the use of equivalent circuit models[52,53] and Jones matrices[54,55], the relationship between the waveform-selective performance and SPICE parameters of diodes remains unclear, which is important for the design of waveform-selective metasurfaces. For this reason, this study reveals how the waveform selectivity is determined by the SPICE parameters used for waveform-selective metasurfaces. In particular, we present simulation results to show how the SPICE parameters are associated with the operating frequency and power of waveform-selective metasurfaces. Thus, our study provides design guidelines for circuit-based waveform-selective metasurfaces to select/fabricate optimal diodes and enhance the waveform-selective performance at the target frequency and power level.

Results

In this study we use the unit cell of the simple waveform-selective metasurface drawn in Fig. 1. In this structure, the unit cell is composed of a square conducting patch, a dielectric substrate (Rogers3003 with loss tangent of 0.0013) and a ground plane (perfect electric conductor: PEC), which resembles unit cells of existing metasurfaces[3]. However, the gap between conducting patches is connected by a set of four Schottky diodes that serve as a full-wave rectifier. Therefore, although the resonant frequency is determined by the same concept as the one that applies to ordinary metasurfaces[3], the incoming waveform following a sine function is fully rectified to generate another waveform based on the modulus of the sine function. In this case, as seen in the Fourier expansion of the rectified waveform, the incoming frequency component is converted to an infinite set of components, although most of the energy is at zero frequency[41,43,44]. For this reason, the circuit configuration drawn in Fig. 1 enables exploitation of the transient phenomena well known in DC circuits even if the incoming waveform is an alternating current (AC) signal. In the particular case shown in Fig. 1, the energy of a short pulse is temporarily stored in the capacitor and then dissipated with the parallel resistor, resulting in strong absorption. If the pulse width is sufficiently long, however, then the capacitor is fully charged such that electric charges induced by the incident wave cannot enter the internal circuit. Thus, the absorption performance is significantly reduced even at the same frequency. Other types of waveform-selective metasurfaces are further explained in the literature[43–45]. In this study, we adopt a co-simulation method available from an ANSYS numerical simulator (Electronics Desktop 2020 R2) to simulate the abovementioned capacitor-based waveform-selective metasurface. Although the co-simulation method is fully explained in the literature[44], we calculate the absorbing performance of the waveform-selective metasurface for long pulses and short pulses in the frequency and time domains, respectively. For the frequency-domain calculation, we use a small signal analysis (for linear simulations) or harmonic balance analysis (for nonlinear simulations), which readily and effectively estimates the absorptance for long signals. For the time-domain calculation, transient reflected energy is calculated and compared to incident energy, which produces transient absorptance for short pulses. Note that the Schottky diodes used in this study are modelled by referring to the SPICE parameters of a commercial product provided by Avago, specifically the HSMS-286x series (Table 1). However, since we vary these SPICE parameters over a wide range, a similar conclusion is expected to be drawn in designing waveform-selective metasurfaces containing other diodes.

First, we numerically studied how the operating frequency of the waveform-selective metasurface can be scaled to a smaller or larger frequency range. Here, we changed the physical design parameters to build simulation models near 280 MHz, 2.8 GHz, 28 GHz and 280 GHz (see the parameters in Table 2). The substrate thickness was adjusted to be almost consistent with the thickness of existing printed circuit board (PCB, Rogers3003) products. Additionally, the incident pulse width was set to 500 ns, 50 ns, 5 ns and 0.5 ns for the 280-MHz, 2.8-GHz, 28-GHz and 280-GHz models, respectively, to maintain the relative bandwidth of the incident pulse (see the literature reporting that the spectrum spreads if the pulse width is too narrow[56]). Before evaluating the waveform-selective response, we simplified the waveform-selective metasurface models to replace all the circuit components with a single 120π-Ω resistor and investigate the operating frequency by using the abovementioned co-simulation method, more specifically the small signal analysis. In this way, the use of the single resistor was useful for clarifying the relationship between the operating frequency and the physical dimensions of the metasurface models as well as the influence of SPICE parameters used later. The simulated absorptances are plotted in Fig. 2, where the absorptance peak appeared at approximately 280 MHz, 2.8 GHz, 28 GHz and 280 GHz, as expected.

After obtaining these results, we conducted a transient analysis to send sufficiently large signals (0 dBm) to the four models. The absorptance of the waveform-selective metasurface was obtained, as shown in Fig. 3. According to this figure, the 280-MHz model and the 2.8-GHz model showed clear differences between the absorptance for short pulses and that for continuous waves (CWs) due to the abovementioned waveform-selective absorption mechanism. However, the 28-GHz model and the 280-GHz model exhibited almost no difference despite the different waveforms and the presence of the rectifying circuit. This occurred because the diodes contained a

Parameter	Variable	Value
Current at breakdown voltage	I_b	1.00×10^{-5} A
Saturation current	I_S	5.00×10^{-8} A
Emission coefficient	N	1.08
Ohmic series resistance	R_S	6 Ω
Reverse breakdown voltage	V_B	7 V
Zero-bias capacitance	C_j	0.18 pF
Multiplier for multiple parallel diodes	M	0
Area junction contact potential	P_B	0.65 V
Energy gap for PN-junction	E_G	0.69 eV
Forward knee current	I_K	0 A/m^2
Reverse knee current	I_{KR}	0 A/m^2

Table 1. SPICE parameters of the Schottky diode model used for waveform-selective metasurfaces.

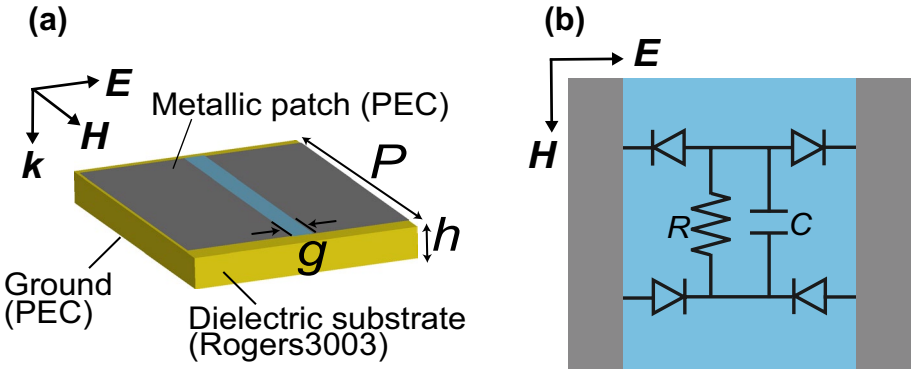

Figure 1. Simulated periodic unit cell model of the waveform-selective metasurface. (**a**) Unit cell and (**b**) circuit deployed between metallic patches. Periodic boundaries were applied in the incident electric and magnetic field directions.

	h (mm)	p (mm)	g (mm)
280-MHz model	15	260	10
2.8-GHz model	1.5	26	1
28-GHz model	0.13	2.7	0.1
280-GHz model	0.015	0.26	0.01

Table 2. Design parameters of waveform-selective metasurfaces.

parasitic junction capacitance C_j, which short-circuited the gap between square patches in the high-frequency region. To readily understand these results, the current flowing into one of the four Schottky diodes was Fourier transformed, as plotted in Fig. 4. These results were obtained in MATLAB by applying a built-in function of the fast Fourier transform (FFT) to only the first 50/5/0.5 ns of the time-domain current in the 2.8/28/280-GHz models. As shown in the insets of Fig. 4, the zero-frequency component of the 280-GHz model was much smaller than that of the 2.8-GHz model (specifically, -94.8 dB in the 280-GHz model and -12.2 dB in the 2.8-GHz model). Since the reactance of C_j approached zero and the diodes no longer rectified induced electric charges, the zero frequency component was severely suppressed in the 280-GHz model. Moreover, the C_j used in SPICE parameters was varied, as shown in Fig. 5, where the difference between the pulse absorptance and CW absorptance was found to increase if C_j was sufficiently small. For instance, when $C_j = 1$ fF, the 280-GHz model exhibited strong absorptance of approximately 0.9 for a short pulse and limited absorptance of less than 0.2 for a CW. Therefore, reducing C_j is very important to distinguish a short pulse from a CW in the high-frequency range. Also, note that this femtofarad-order parasitic capacitance is too small as ordinary commercial products but is realizable as customized integrated circuit chips[57].

Another point here is that the 280-GHz model had a very small gap of 0.015 mm between conducting patches. This indicates that the loaded circuit components, including diodes, must be smaller than 0.015 mm. From the

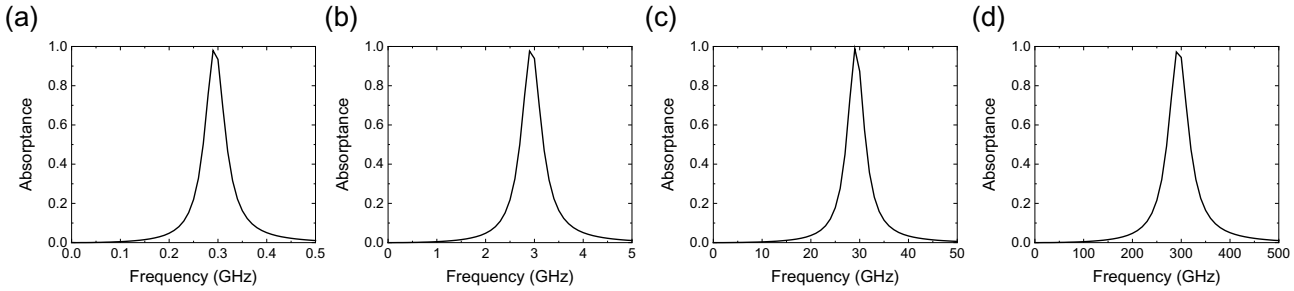

Figure 2. Frequency-domain absorption profiles of simulation models using only an 120π-Ω resistor in the conductor gap without a diode bridge or a capacitor: (**a**) 280-MHz, (**b**) 2.8-GHz, (**c**) 28-GHz and (**d**) 280-GHz models.

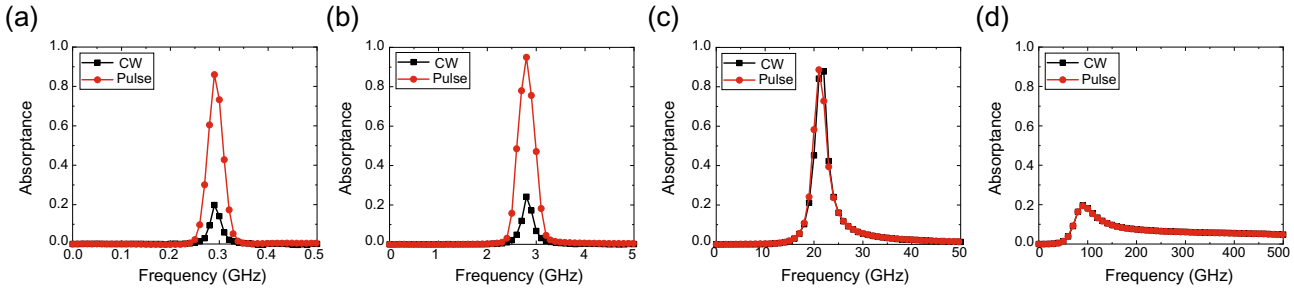

Figure 3. Frequency-domain absorption profiles of simulation models using all the circuit components for high-power signals: (**a**) 280-MHz, (**b**) 2.8-GHz, (**c**) 28-GHz and (**d**) 280-GHz models. The input power was set to 0 dBm.

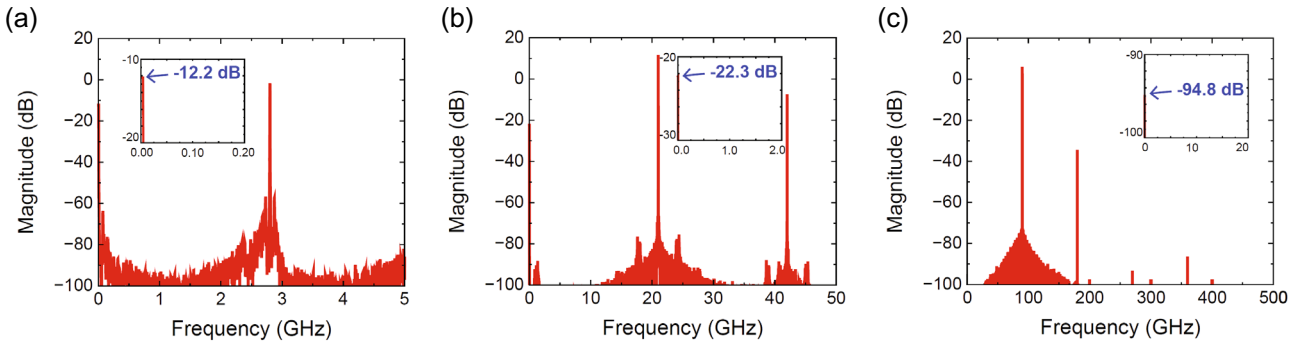

Figure 4. Spectrum of the current at one of diodes used in the waveform-selective metasurface. (**a**) 2.8-GHz, (**b**) 28-GHz and (**c**) 280-GHz models. The insets represent the spectrum near zero frequency. The oscillation frequencies of the 2.8-GHz, 28-GHz and 280-GHz models were fixed at 2.8, 21 and 90 GHz, respectively, where the transmittance was most enhanced in Fig. 3. The input power was set to 0 dBm.

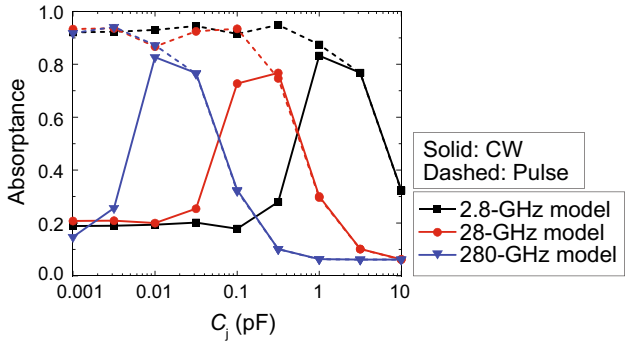

Figure 5. Relationship between absorptance and C_j. The frequencies of the 2.8-GHz, 28-GHz and 280-GHz models were adjusted to maximize the transmittance. The input power was set to 0 dBm.

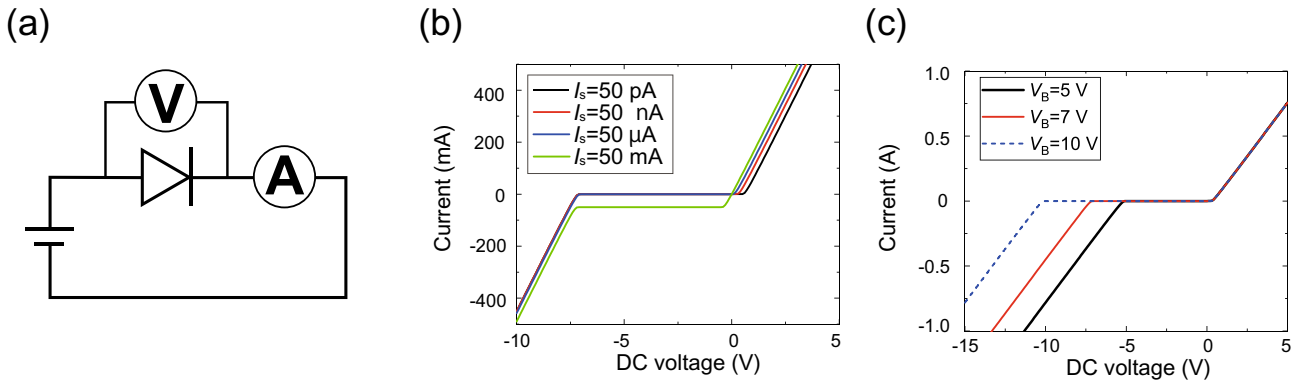

Figure 6. Influence of saturation current I_S and breakdown voltage V_B. (**a**) Circuit schematic. *IV* curves with various (**b**) I_Ss and (**c**) V_Bs.

viewpoint of semiconductor fabrication, small diode chips can be fabricated by using the stealth dicing technique if the chip dimensions are 0.1 mm or larger[58]. To further reduce the chip dimensions, directly fabricating conducting patterns of metasurfaces on chips, namely, not on PCBs, is more realistic[59,60]. Additionally, C_j can be reduced to the femtofarad order, as plotted in Fig. 5[59]. However, this does not necessarily ensure that other diode characteristics such as optimal turn-on voltage and current are realized in this power range. Therefore, reaching a balance between C_j and other parameters is important to optimize the performance of waveform-selective metasurfaces in the high-frequency range.

Next, we investigated how the operating power level is determined by the SPICE parameters. To readily understand the relationship between the operating power level and diode properties, first, we plotted simple *IV* curves of a single diode biased by a DC source, as drawn in Fig. 6a, where we changed saturation current I_S and breakdown voltage V_B. According to Fig. 6b, the turn-on voltage was decreased by increasing I_S. At the same time, however, increasing I_S allowed an increase in the backward current. Additionally, Fig. 6c shows that V_B simply determined the voltage to break down the diode. Specifically, the larger V_B was, the larger the voltage that could be applied across the diode without current leakage.

Based on the simulation results in Fig. 6, we then varied the I_S and V_B of the waveform-selective metasurface, as plotted in Fig. 7. Note that in this figure we used the 2.8-GHz model simulated in Fig. 3. Figure 7 shows that by increasing I_S, strong absorption was obtained for short pulses with a small power level (e.g., near -10 dBm with I_S set to 0.5 nA). At the same time, however, the CW absorptance gradually increased since, as shown in Fig. 6b, the diodes permitted more electric charge to come in from the backward direction as well. In addition, Fig. 7 indicates that by increasing V_B, the CW absorptance was suppressed for a wider range of the input power. This figure shows that if the CW absorptance starts increasing, then the input power exceeds the breakdown voltage of the diodes. We also varied other parameters such as forward knee current I_K and backward knee current I_{KR}, each of which is related to the amount of current at the turn-on voltage and the breakdown voltage, respectively. Changes in I_K and I_{KR} also determine the waveform-selective response, as shown in Fig. 7.

In Fig. 7, we clarified how the operating power range was associated with I_S and V_B. However, the difference between the pulse absorptance and the CW absorptance was maximized only in a narrow power range (e.g., around 0 dBm in Fig. 7b). This occurred because this dynamic range was constrained by the change in the resistive component of the diodes[61]. More specifically, the entire metasurface impedance including the diode resistance matched the wave impedance of free space to maintain the large absorptance for short pulses in a limited

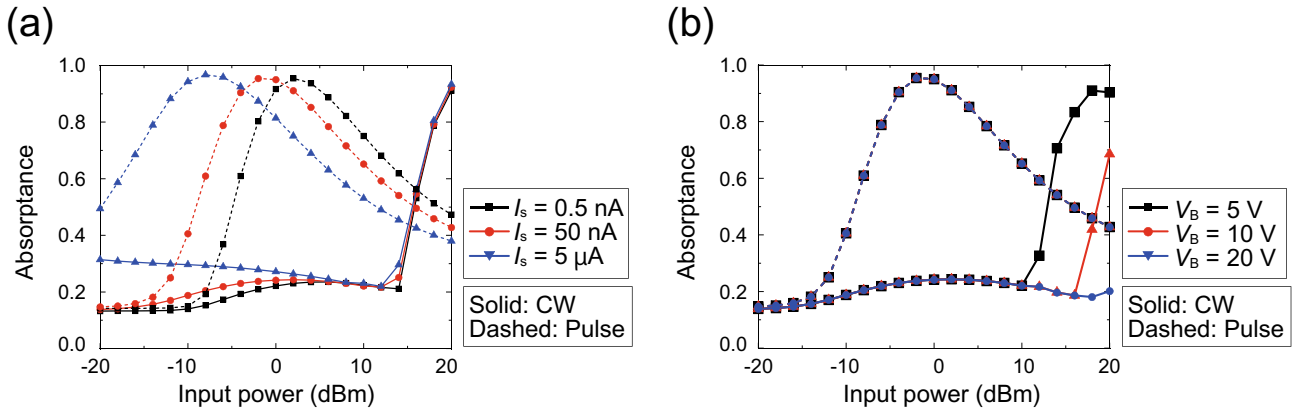

Figure 7. Relationship between absorptance and I_S or V_B in the 2.8-GHz model. Absorptance with various (**b**) I_Ss and (**c**) V_Bs. The frequency and input power were fixed at 2.8 GHz and 0 dBm, respectively.

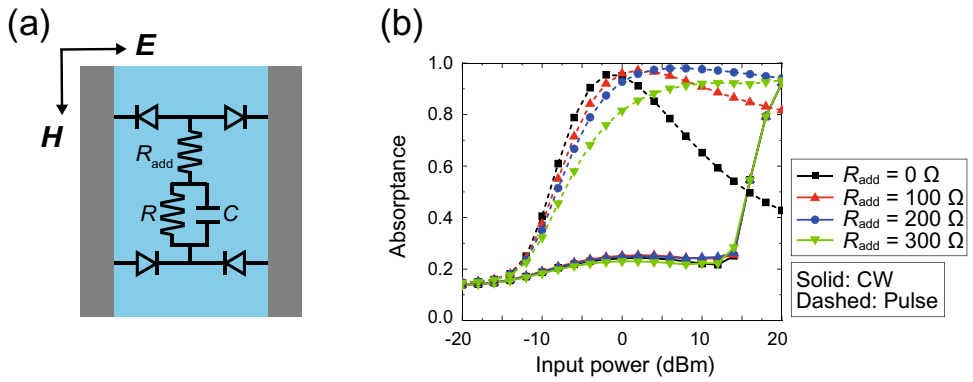

Figure 8. Use of an additional series resistance R_{add} to improve the dynamic range of the 2.8-GHz model. (**a**) Configuration of the circuit deployed between conductor edges. This circuit was deployed between conducting ptaches (see Fig. 1a). (**b**) Absorptance with various R_{add}s. The frequency and input power were fixed at 2.8 GHz and 0 dBm, respectively.

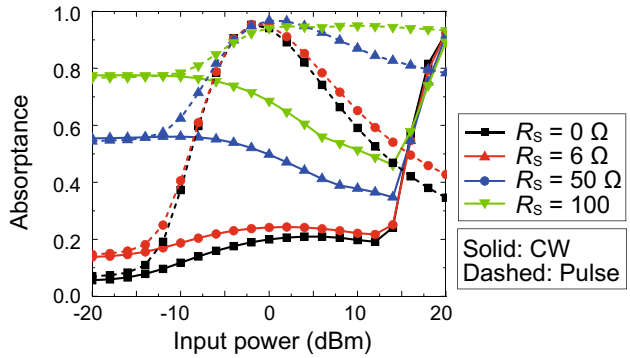

Figure 9. Absorptance with various R_Ss in the 2.8-GHz model. The frequency and input power were fixed at 2.8 GHz and 0 dBm, respectively.

power range, since the resistive component of the diodes largely varied in response to the power level of the incoming wave. To address this issue and minimize the influence of the resistive component of the diodes, one may add an additional series resistance R_{add} to the inside of the diode bridge, as drawn in Fig. 8a. In this case, the resistive component of the diodes still varies with the input power. However, the influence can be almost ignored if R_{add} is moderately large. For this reason, the difference between the pulse absorptance and the CW absorptance was maintained at 0.7 or higher from 0 to 14 dBm when R_{add} was set to 200 Ω, as shown in Fig. 8b. Thus, the dynamic range of the waveform selectivity can be readily broadened by adjusting R_{add}.

Moreover, the parasitic series resistive component of the diodes R_S relates to the dynamic range of the waveform-selective metasurface to some extent. This is seen in Fig. 9, where R_S was changed from 0 to 100 Ω. The absorptance for the short pulse was as large as 0.9 between 0 and 20 dBm when R_S was 100 Ω, which was similar to the pulse absorptance with R_{add} = 200 Ω in Fig. 8b. However, the absorptance for the CW was also increased in the same power range because R_S was involved in not only the rectification process required for the waveform selectivity but also the intrinsic resonance mechanism of the patch structure (see the structure showing large absorptance in Fig. 2). Therefore, including a resistive component inside the diode bridge as R_{add} is important to increase the absorptance for short pulses but not CWs.

This study numerically unveiled how SPICE parameters of diodes are related to the performance of waveform-selective metasurfaces that are capable of varying electromagnetic response in accordance with the pulse width of incoming waves even at the same frequency. This study only focused on numerical evaluation since measurements add additional complexities to the assessment (e.g. additional parasitic parameters). We note that our simulations were fully based on the co-simulation method of Ansys Electronics Desktop, namely, one of commercial software products widely used and verified by measurements already[41,43,44,47,49,50]. However, the experimental validation is still important to assess the practical performance of waveform-selective metasurfaces with various SPICE parameters, which can be further explored as a future subject. Here we note that the design of the entire circuit configuration is highly customizable. For instance, our study assumed R_{add} as a discrete lumped component, which in practice leads to adding an additional inductive component due to the soldering. However, this parasitic component can be suppressed by integrating R_{add} with diodes as a single packaged chip. In other words, additional parasitic components appearing in measurements highly depend on the circuit design.

Conclusion

In this study, we investigated how the absorption profiles of waveform-selective metasurfaces are related to their SPICE parameters. In particular, we have drawn conclusions about how the SPICE parameters are related to (1) the high-frequency operation, (2) input power requirement and (3) dynamic range of waveform-selective metasurfaces with supporting simulation results. First, we clarified the relationship between the SPICE parameters and the operating frequency. The operating frequencies of conventional metasurfaces that do not include circuit components are well known to be adjusted by simply varying the physical dimensions. In the case of waveform-selective metasurfaces, however, junction capacitance C_j was shown to play an important role in the high-frequency range in maintaining the difference between the absorptance for a short pulse and that for a CW. Second, we showed how the operating power level of the waveform-selective metasurfaces is determined by the SPICE parameters. Our simulation results showed that saturation current I_S and breakdown voltage V_B are important for reducing the operating power level and maintaining small absorptance up to a large input power level, respectively. However, these two parameters were found to not contribute to broadening of the dynamic range of the waveform-selective metasurfaces, which can be improved by introducing an additional resistive component R_{add} into the inside of the diode bridge. Thus, our study is expected to provide design guidelines for circuit-based waveform-selective metasurfaces to select/fabricate optimal diodes and enhance the waveform-selective performance at the target frequency and power level. Our results are usefully exploited to ensure the selectivity based on the pulse duration of the incident wave in a range of potential applications including electromagnetic interference, wireless power transfer, antenna design, wireless communications, and sensing.

Data availibility

All data generated or analysed during this study are included in this published article.

Received: 26 December 2022; Accepted: 24 April 2023
Published online: 03 May 2023

References

1. Engheta, N. & Ziolkowski, R. *Metamaterials Physics and Engineering Explorations* (IEEE Press, Wiley, Piscataway, 2006).
2. Smith, D. R., Padilla, W. J., Vier, D. C., Nemat-Nasser, S. C. & Schultz, S. Composite medium with simultaneously negative permeability and permittivity. *Phys. Rev. Lett.* **84**, 4184–4187 (2000).
3. Sievenpiper, D., Zhang, L., Broas, R. F. J., Alexopolous, N. G. & Yablonovitch, E. High-impedance electromagnetic surfaces with a forbidden frequency band. *IEEE Trans. Microw. Theory Tech.***47**, 2059–2074 (1999).
4. Yu, N. *et al.* Light propagation with phase discontinuities: Generalized laws of reflection and refraction. *Science* **334**, 333–337 (2011).
5. Yu, N. & Capasso, F. Flat optics with designer metasurfaces. *Nat. Mater.* **13**, 139–150 (2014).
6. Shelby, R. A., Smith, D. R., Nemat-Nasser, S. C. & Schultz, S. Microwave transmission through a two-dimensional, isotropic, left-handed metamaterial. *Appl. Phys. Lett.* **78**, 489–491 (2001).
7. Pendry, J. B., Schurig, D. & Smith, D. R. Controlling electromagnetic fields. *Science* **312**, 1780–1782 (2006).
8. Schurig, D. *et al.* Metamaterial electromagnetic cloak at microwave frequencies. *Science* **314**, 977–980 (2006).
9. Pendry, J. B. Negative refraction makes a perfect lens. *Phys. Rev. Lett.* **85**, 3966–3969 (2000).
10. Fang, N., Lee, H., Sun, C. & Zhang, X. Sub-diffraction-limited optical imaging with a silver superlens. *Science* **308**, 534–537 (2005).
11. Landy, N. I., Sajuyigbe, S., Mock, J. J., Smith, D. R. & Padilla, W. J. Perfect metamaterial absorber. *Phys. Rev. Lett.* **100**, 207402 (2008).
12. Kern, D. J. & Werner, D. H. A genetic algorithm approach to the design of ultra-thin electromagnetic bandgap absorbers. *Microwave Opt. Technol. Lett.* **38**, 61–64 (2003).
13. Wakatsuchi, H., Greedy, S., Christopoulos, C. & Paul, J. Customised broadband metamaterial absorbers for arbitrary polarisation. *Opt. Express* **18**, 22187–22198 (2010).
14. Watts, C. M., Liu, X. & Padilla, W. J. Metamaterial electromagnetic wave absorbers. *Adv. Mater.***24**, OP98–OP120 (2012).
15. Ziolkowski, R. W., Jin, P. & Lin, C.-C. Metamaterial-inspired engineering of antennas. *Proc. IEEE* **99**, 1720–1731 (2011).
16. Barbuto, M. *et al.* Metasurfaces 3.0: a new paradigm for enabling smart electromagnetic environments. *IEEE Trans. Antennas Propag.* (2021).
17. Silva, A. *et al.* Performing mathematical operations with metamaterials. *Science* **343**, 160–163 (2014).
18. Mohammadi Estakhri, N., Edwards, B. & Engheta, N. Inverse-designed metastructures that solve equations. *Science* **363**, 1333–1338 (2019).
19. Zangeneh-Nejad, F., Sounas, D. L., Alù, A. & Fleury, R. Analogue computing with metamaterials. *Nat. Rev. Mater.* **6**, 207–225 (2021).
20. Sievenpiper, D. F., Schaffner, J. H., Song, H. J., Loo, R. Y. & Tangonan, G. Two-dimensional beam steering using an electrically tunable impedance surface. *IEEE Trans. Antennas Propag.* **51**, 2713–2722 (2003).
21. Pfeiffer, C. & Grbic, A. Metamaterial huygens' surfaces: Tailoring wave fronts with reflectionless sheets. *Phys. Rev. Lett.* **110**, 197401 (2013).
22. Shaltout, A. M. *et al.* Spatiotemporal light control with frequency-gradient metasurfaces. *Science* **365**, 374–377 (2019).
23. Wu, Q. & Zhang, R. Towards smart and reconfigurable environment: Intelligent reflecting surface aided wireless network. *IEEE Commun. Mag.* **58**, 106–112 (2019).
24. Di Renzo, M. *et al.* Smart radio environments empowered by reconfigurable intelligent surfaces: How it works, state of research, and the road ahead. *IEEE J. Sel. Areas Commun.* **38**, 2450–2525 (2020).
25. Gradoni, G. *et al.* Smart radio environments. arXiv preprint arXiv:2111.08676 (2021).
26. Chen, H. *et al.* Active terahertz metamaterial devices. *Nature* **444**, 597–600 (2006).
27. Zharov, A. A., Shadrivov, I. V. & Kivshar, Y. S. Nonlinear properties of left-handed metamaterials. *Phys. Rev. Lett.* **91**, 37401 (2003).
28. Lapine, M., Shadrivov, I. V. & Kivshar, Y. S. Colloquium: Nonlinear metamaterials. *Rev. Mod. Phys.* **86**, 1093 (2014).
29. Li, A., Luo, Z., Wakatsuchi, H., Kim, S. & Sievenpiper, D. F. Nonlinear, active, and tunable metasurfaces for advanced electromagnetics applications. *IEEE Access* **5**, 27439–27452 (2017).
30. Wakatsuchi, H., Kim, S., Rushton, J. J. & Sievenpiper, D. F. Circuit-based nonlinear metasurface absorbers for high power surface currents. *Appl. Phys. Lett.* **102**, 214103 (2013).
31. Kim, S., Wakatsuchi, H., Rushton, J. J. & Sievenpiper, D. F. Switchable nonlinear metasurfaces for absorbing high power surface waves. *Appl. Phys. Lett.* **108**, 041903 (2016).

32. Li, A. *et al.* High-power transistor-based tunable and switchable metasurface absorber. *IEEE Trans. Microw. Theory Tech.* **65**, 2810–2818 (2017).
33. Zhou, L., Liu, L. & Shen, Z. High-performance energy selective surface based on the double-resonance concept. *IEEE Trans. Antennas Propag.* **69**, 7658–7666 (2021).
34. Yang, C., Liu, P. G. & Huang, X. J. A novel method of energy selective surface for adaptive HPM/EMP protection. *IEEE Antennas Wirel. Propag. Lett.* **12**, 112–115 (2013).
35. Zhao, C., Wang, C. F. & Aditya, S. Power-dependent frequency-selective surface: Concept, design, and experiment. *IEEE Trans. Antennas Propag.* **67**, 3215–3220 (2019).
36. Kiani, M., Momeni, A., Tayarani, M. & Ding, C. Spatial wave control using a self-biased nonlinear metasurface at microwave frequencies. *Opt. Express* **28**, 35128–35142 (2020).
37. de Lustrac, A., Ratni, B., Piau, G., Duval, Y. & Burokur, S. N. Tri-state metasurface-based electromagnetic screen with switchable reflection, transmission, and absorption functionalities. *ACS Appl. Electron. Mater.* **3**, 1184–1190 (2021).
38. Luo, Z. & others Intensity-dependent metasurface with digitally reconfigurable distribution of nonlinearity. *Adv. Opt. Mater.***7**, 1900792 (2019).
39. Zhang, L. *et al.* Space-time-coding digital metasurfaces. *Nat. Commun.* **9**, 1–11 (2018).
40. Zhang, L. *et al.* A wireless communication scheme based on space-and frequency-division multiplexing using digital metasurfaces. *Nat. Electron.* **4**, 218–227 (2021).
41. Wakatsuchi, H., Kim, S., Rushton, J. J. & Sievenpiper, D. F. Waveform-dependent absorbing metasurfaces. *Phys. Rev. Lett.* **111**, 245501 (2013).
42. Eleftheriades, G. V. Electronics: Protecting the weak from the strong. *Nature* **505**, 490–491 (2014).
43. Wakatsuchi, H. *et al.* Waveform selectivity at the same frequency. *Sci. Rep.* **5**, 9639 (2015).
44. Wakatsuchi, H., Long, J. & Sievenpiper, D. F. Waveform selective surfaces. *Adv. Func. Mater.* **29**, 1806386 (2019).
45. Vellucci, S., Monti, A., Barbuto, M., Toscano, A. & Bilotti, F. Waveform-selective mantle cloaks for intelligent antennas. *IEEE Trans. Antennas Propag.* **68**, 1717–1725 (2019).
46. Barbuto, M. *et al.* Waveguide components and aperture antennas with frequency-and time-domain selectivity properties. *IEEE Trans. Antennas Propag.* **68**, 7196–7201 (2020).
47. Ushikoshi, D. *et al.* Pulse-driven self-reconfigurable meta-antennas. *Nat. Commun.* **14**, 633 (2023).
48. Fathnan, A. A., Homma, H., Sugiura, S. & Wakatsuchi, H. Method for extracting the equivalent admittance from time-varying metasurfaces and its application to self-tuned spatiotemporal wave manipulation. *J. Phys. D Appl. Phys.* **55**, 015304 (2022).
49. Tashiro, M., Fathnan, A. A., Sugiura, Y., Uchiyama, A. & Wakatsuchi, H. Metasurface-inspired maintenance-free internet of things tags characterised in both frequency and time domains. *Electron. Lett.* **58**, 937–939 (2022).
50. Ushikoshi, D. *et al.* Experimental demonstration of waveform-selective metasurface varying wireless communication characteristics at the same frequency band of 2.4 ghz. *Electron. Lett.***56**, 160–162 (2020).
51. F. Imani, M. & Smith, D. R. Temporal microwave ghost imaging using a reconfigurable disordered cavity. *Appl. Phys. Lett.***116**, 054102 (2020).
52. Baena, J. D. *et al.* Equivalent-circuit models for split-ring resonators and complementary split-ring resonators coupled to planar transmission lines. *IEEE Trans. Microw. Theory Tech.* **53**, 1451–1461 (2005).
53. Wakatsuchi, H., Paul, J., Greedy, S. & Christopoulos, C. Cut-wire metamaterial design based on simplified equivalent circuit models. *IEEE Trans. Antennas Propag.* **60**, 3670–3678 (2012).
54. Li, J. *et al.* Hybrid dispersion engineering based on chiral metamirror. *Laser Photon. Rev.* **17**, 2200777 (2023).
55. Yuan, Y., Wu, Q., Burokur, S. N. & Zhang, K. Chirality-assisted phase metasurface for circular polarization preservation and independent hologram imaging in microwave region. *IEEE Trans. Microw. Theory Tech.*
56. Wakatsuchi, H. Time-domain filtering of metasurfaces. *Sci. Rep.* **5**, 16737 (2015).
57. Chew, K. W. J. *et al.* RF performance of 28nm PolySiON and HKMG CMOS devices. *2015 IEEE Radio Frequency Integrated Circuits Symposium (RFIC)* 43–46 (2015).
58. Kumagai, M. *et al.* Advanced dicing technology for semiconductor waferŮstealth dicing. *IEEE Trans. Semicond. Manuf.* **20**, 259–265 (2007).
59. Froment, B. *et al.* New interconnect capacitance characterization method for multilevel metal CMOS processes. *Proceedings of the IEEE 1999 International Interconnect Technology Conference* 224–226 (1999).
60. Venkatesh, S. *et al.* A high-speed programmable and scalable terahertz holographic metasurface based on tiled CMOS chips. *Nat. Electron.* **3**, 785–793 (2020).
61. Asano, K., Nakasha, T. & Wakatsuchi, H. Simplified equivalent circuit approach for designing time-domain responses of waveform-selective metasurfaces. *Appl. Phys. Lett.* **116**, 171603 (2020).

Acknowledgements

This work was supported in part by the National Institute of Information and Communications Technology (NICT), Japan under the commissioned research No. 06201, the Japan Science and Technology Agency (JST) under the Precursory Research for Embryonic Science and Technology (PRESTO) No. JPMJPR193A and the Japanese Ministry of Internal Affairs and Communications (MIC) under the Strategic Information and Communications R &D Promotion Program (SCOPE) No. 192106007.

Author contributions

H.W. designed the entire project. S.I., H.H. and M.T. jointly conducted numerical simulations and analysed the results. H.W., A.A.F., C.Y., J.N, M.K., Y.O. and K.N. also considered the results. All authors reviewed the manuscript.

Competing interests

The authors declare no competing interests.

Additional information

Correspondence and requests for materials should be addressed to H.W.